3D Printing of Sustainable Coal Polymer Composites: Study of Processing, Mechanical Performance, and Atomistic Matrix−Filler Interaction

Logan E. Veley,* Chinonso Ugwumadu, Jason P. Trembly, David A. Drabold, and Yahya Al-Majali*

Cite This: https://doi.org/10.1021/acsapm.3c01784

Read Online

ACCESS		📊 Metrics & More		📖 Article Recommendations		🗐 Supporting Information

ABSTRACT: Bituminous coal was utilized as a particulate filler in polymer-based composites to fabricate standard 1.75 mm coal-plastic composite filaments for material extrusion 3D printing. The composites were formulated by incorporating Pittsburgh No. 8 coal into polylactic acid, polyethylene terephthalate glycol, high-density polyethylene, and polyamide-12 resins with loadings ranging from 20 to 70 wt %. Coal-plastic composite filaments were extruded and printed by using the same processing parameters as the respective neat plastics. The introduction of coal ameliorated the warping problem of 3D printed high-density polyethylene, allowing for additive manufacturing of an inexpensive and widely available thermoplastic. The mechanical properties of the 3D printed composites were characterized and compared to those of composites fabricated using traditional compression molding. Microscopy of as-fractured samples revealed that particle pull-out and particle fracture were the predominant modes of composite failure. Tensile and flexural moduli as well as hardness had direct proportionality with increasing coal content, while flexural strength, tensile strength, and impact resistance decreased for most composite formulations. Interestingly, polyamide-based composites demonstrated greater maximum tensile and flexural strengths than unfilled plastic. Investigation of composite interfacial chemistry via molecular dynamics simulations and Fourier-transform spectroscopy revealed beneficial hydrogen bonding interactions between coal and polyamide-12, while no chemical reactions were evident for the other polymers investigated.

KEYWORDS: *coal-plastic composite, additive manufacturing, fused deposition modeling, material extrusion, molecular dynamics simulation*
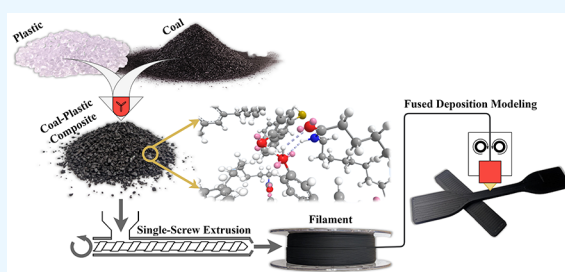
1. INTRODUCTION

Fused deposition modeling (FDM) is a material extrusion additive manufacturing (AM) technique where thermoplastic filaments are extruded through a heated nozzle along a desired path to build a three-dimensional object layer by layer.[1] FDM provides an avenue for rapid prototyping and part production with minimal waste, but its applications have been restricted by poor mechanical performance due to limited polymer chain entanglement across print layers.[1] Despite these limitations, FDM has been shown as a viable route to enter the composite tooling market which had a global value of $493 million in 2022.[2,3] The development of sustainable and profitable FDM materials yields further market adoption of AM composite tooling.

Arguably the greatest advantage of FDM is the vast array of materials available in the form of 1.75 mm filaments for printing.[1] Common polymers processed via FDM include polylactic acid (PLA), polyethylene terephthalate glycol (PETG), and acrylonitrile butadiene styrene (ABS).[1] High-performance parts are frequently printed from polymers such as polyamide-12 (PA12), commonly known as nylon-12. Some commodity plastics, however, present noticeable challenges when processed via FDM. For example, high-density poly-ethylene (HDPE) is rarely used in FDM applications due to poor layer adhesion, warping, and shrinkage.[4,5]

Polymer composite filaments are also processed via FDM. Particulate fillers and chopped fibers are added to the polymer filaments for aesthetic and structural purposes. Wood flour has been used to imitate wooden structures and improve sustainability compared to printing neat plastic.[6−10] Copper or other metal-filled filaments utilize the polymer resin as a binder to 3D print structures that can be sintered into metallic parts.[6] Most commonly, chopped glass or carbon fibers are combined with polyamide resins to produce composite filaments with improved strength and wear characteristics.[11]

However, synthetic fibers are relatively expensive, energy-intensive to produce, and abrasive to processing equipment.

Recently, coal-filled thermoplastic composite materials have been investigated for utilization in high-volume applications such as building materials.[12−14] Compared to wood-plastic composites (WPCs), predominantly utilized as decking boards, coal-plastic composite (CPC) materials possessed comparable or higher mechanical performance, higher oxidation resistance (i.e., longer service life), greater thermal stability and flammability resistance, lower embodied energy and emissions, and lower production costs.[13−16]

Currently, the development of CPC materials has been primarily limited to traditional extrusion-based manufacturing processes. Leveraging the composite's benefits via alternative manufacturing processes such as AM provides the opportunity to further expand the technology to new applications and industries including composite tooling and additive house construction. While Zhang et al. successfully demonstrated the processing of PA12 CPC filaments filled with up to 20 wt % anthracite and 50 wt % lignite coals, common FDM plastics, such as PLA and PETG, and other widely available and inexpensive plastics, such as HDPE, were not explored.[17] The performance and economic benefits of CPC materials can be further compounded by leveraging AM. Developing CPC filaments with high coal filler contents and characterizing their mechanical performance provide the opportunity to create sustainable and economically viable feedstocks for 3D printing tooling and structural components.

Over the years, experimental studies on materials have provided valuable insights into the chemical, thermal, and mechanical properties of materials as well as their local atomic ordering. However, determining the unique atomic structure of organic materials like coal and plastics only through experiments is challenging and requires complex analysis for interpretation.[18] To overcome this limitation, validated computer models based on experimental data have emerged as a reliable approach to obtaining atomistic information and understanding the physical properties of materials at different scales, ranging from the intramolecular to supramolecular levels. While the structures and properties of many plastics with a crystalline nature are well-known,[19,20] accurately predicting the structures of amorphous carbon-based materials, ranging from ordered structures like amorphous graphene,[21,22] fullerenes,[23] and nanotubes,[24] to complex coal structures, has been a topic of significant research interest.

Due to the complex formation process of coal, coupled with the presence of noncarbon elements like H, O, N, and S, there are over 133 molecular representations of coal (or coal extracts) available,[25,26] including notable models such as the Wiser,[27] Wender,[28] Given,[29] and Shinn[30] models, which provide general or specific descriptions of coal structure. For example, Solomon's model provides a structural description of Pittsburgh No. 8 (P8) coal by combining experimental investigations and thermal decomposition data.[31] While there have been numerous independent atomistic descriptions of coal and plastics using molecular simulations, to the best of the authors' knowledge, no published work has focused on the molecular simulation of CPCs.

The objective of this research was to develop 3D printable CPC materials and investigate the composites' behavior. CPC FDM filaments were developed to maximize the coal filler content, and the respective printing parameters were identified. CPC materials made with PLA, PETG, HDPE, and PA12

resins were characterized. A foundational understanding of the mechanical response of the CPC materials is critical for the development of the technology for future industrial applications, such as additive housing construction or large-scale composite tooling manufacturing. The tensile and flexural strength and moduli are fundamental for design in structural applications, and impact resistance provides insights into the materials' energy dissipation. The hardness of the materials characterizes the CPCs for wearing environments. Furthermore, the interactions between coal and plastics were studied via molecular dynamics simulations involving atomistic models of P8 coal, plastics, and composites. Avogadro[32] and ChemDraw were utilized to build the atomistic models, and various simulation techniques such as plane-wave basis density functional theory (DFT),[33] reactive force field (REAXFF),[34] and molecular mechanics force fields (MM3)[35] were employed. Quantification of the composites' mechanical properties, processing parameters, and molecular interactions is essential for future technology development and adoption.

2. METHODOLOGY

2.1. Experimental Section. *2.1.1. Materials.* CPC filaments were derived from virgin plastic pellets and a bituminous coal filler. PLA (PPLA110000, $\rho = 1.24$ g/cm^3) and PETG (PPTG110000, $\rho = 1.24$ g/cm^3) pellets were sourced from 3DXTECH. Paxon EA55-003 HDPE pellets ($\rho = 1.24$ g/cm^3) were supplied by ExxonMobil, and PA12 pellets (044, $\rho = 1.02$ g/cm^3) were obtained from Scientific Polymer Products Inc. Struktol TPW 104 processing additive was used as a lubricant for processing HDPE filaments. Bituminous P8 coal was supplied by CONSOL Energy.

2.1.2. Material Synthesis. Composite formulations containing 20−70 wt % coal were developed based on successful filament extrusion trials from the different matrix resins. P8 coal was pulverized and sieved below a particle size of 38 μm. The coal powder was dried in a convection oven at 110 °C for 24 h to decrease the moisture content to less than 1 wt %. Dried coal (20−70 wt %) and balance matrix resins were melt-mixed for 5 min at 100 rpm using a Rheomix 600 batch mixer. Processing additives (i.e., 1 wt % Struktol TPW 104 for HDPE composites) were introduced during this step. Based on the resin type, CPC materials were compounded at temperatures ranging from 180 to 210 °C. The compounded CPC materials were ground using a Retsch SM 100 cutting mill and were stored in a desiccator for further processing.

2.1.3. Filament Extrusion and FDM Printing. CPC pellets were extruded into filaments using a 3devo Composer 450 and a Filabot Ex2 single-screw filament extruder. The materials were processed at barrel temperatures ranging from 175 to 230 °C. The filaments were drawn to a 1.75 mm diameter before being air-cooled.

Subsequently, CPC filaments were 3D printed (3DP) by using a FlashForge Creator Pro FDM printer. Mechanical test samples were printed in the horizontal orientation with 0−90° linear infill to promote isotropic behavior for comparison to traditionally manufactured samples. The print orientation is shown in Figure S1 of the Supporting Information. The printing parameters, the print temperatures, and the bed adhesion methods for each matrix resin are provided in Tables S1 and S2 of the Supporting Information.

2.1.4. Compression Molding. For characterization of the intrinsic filament composite material and for comparison to the as-printed state, CPC pellets were compression-molded (CM)

to produce samples for mechanical testing. A model 3912 Carver Press was used to compression mold 200 mm × 200 mm × 3.5 mm sheets from aluminum molds coated with a Frekote 770-NC mold release agent. The materials were heated at 180 to 195 °C for 20 min prior to pressing to 8 metric tons for 5 min. The sheets were allowed to cool in air in the mold. Type IV tensile, flexural, and Izod impact resistance samples were cut from the composite sheets by using a ProtoMAX water-jet cutter.

2.1.5. Mechanical Testing. Tensile and flexural tests were performed using an Instron 5966 load frame. Tensile tests were conducted according to ASTM D638.[36] Type IV tensile samples were tested at a displacement rate of 5 mm/min, and a one-inch clip-on extensometer was used to measure the sample strain. Three-point flexural testing was performed in accordance with ASTM D790 procedure B using a span-to-thickness ratio of 16.[37] All stresses are reported as engineering stresses, and the tensile and flexural moduli values were estimated by using linear regression.

Izod impact resistance tests were performed using an Instron CEAST 9050 pendulum impact machine. Izod impact samples were notched using an Instron notching fixture, and notched Izod tests were performed according to ASTM D256 Test Method A.[38]

Composite hardness was determined using a Gain Express 560-10D Shore D hand-held durometer. For all mechanical tests, a minimum of six samples were tested.

2.1.6. Microscopy. Optical microscopy was performed using a Keyence VHX-7000 digital microscope to investigate the coal dispersion and the composite microstructure. A JEOL JSM-6390LV scanning electron microscope was used to investigate the matrix−filler interface. As-fractured flexural samples were sputter coated with gold at 20 mA for 180 s. Images at 1000× magnification were captured using an accelerating voltage of 15 kV. Scanning electron microscopy (SEM) images were used to identify mechanical failure mechanisms present in the composite.

2.1.7. Fourier-Transform Infrared Spectroscopy. Attenuated total reflection Fourier-transform infrared spectroscopy (FTIR) was conducted using a Thermo Scientific Nicolet 6700. Composite disc samples were CM by using stainless steel ring molds and polytetrafluoroethylene platen sheets. Thin composite sheets (0.25 mm thick) were tested by using a diamond ZnSe crystal.

2.2. Simulation of P8 Coal, Plastics, and CPC Models. Representative models for the matrix materials (PLA, PETG, HDPE, and PA12), filler (P8 coal), and their composite models were constructed using ChemDraw and Avogadro. To ensure the accuracy and reliability of the simulations, an extensive ensemble of structural models was analyzed, involving statistically meaningful sampling of the configuration space of the material of interest. For this purpose, 20 coal models ($C_{166}H_{138}O_{15}N_2S_2$) were manually built based on the 2D structure for Pittsburgh bituminous coal proposed by Solomon[31,39] (see the representative model in Figure S2a). At first, the aliphatic and aromatic structures in each P8 coal model were constructed in a 3D box. Subsequently, the MM3 force field, as implemented in ChemDraw and Avogadro, was used for the conformation optimization and energy minimization of the constructed models. Supercell models containing 20 units of P8 coal were generated using the PACKMOL software package[40] (see the representative 3D coal model in Figure S3b). The final models were subsequently

validated using DFT and REAXFF potentials via a conjugate gradient relaxation. DFT calculations were implemented within the Vienna Ab initio Simulation Package (VASP)[33] with the projector augmented wave (PAW) method[41] and the Perdew−Burke−Ernzerhof (PBE) exchange−correlation functional.[42] The REAXFF calculations were performed using the large-scale atomic/molecular massively parallel simulator (LAMMPS).[43] In all of the models (coal and plastics), hydrogen, carbon, nitrogen, oxygen, and sulfur atoms were colored white, gray, blue, red, and yellow, respectively.

The plastics were constructed from scratch using Chem-Draw, with monomers repeated 100 times. Figure S3 depicts atomic structure representations of the different plastics investigated in this study. The PACKMOL algorithm was used to construct the CPC models, ensuring a minimum pairwise distance of about 3 Å between atoms from different molecules to prevent disruptive van der Waals repulsive interactions and atom overlap in the initial configurations. To simulate the laboratory process of melt-mixing the plastic and coal, the composite models were heated in a canonical ensemble that was controlled by a Nose−Hoover thermostat[44,45] at a temperature of 200 °C. Subsequently, the models were optimized to reach an energy minimal configuration using the conjugate gradient implementation. The REAXFF interatomic potential was employed in the simulated melt-mixing protocol with a time step of 0.25 fs to account for the high-frequency dynamics of the hydrogen atoms in the models.

3. RESULTS AND DISCUSSION

3.1. Experimental Results. *3.1.1. CPC Filament Processing.* CPC filaments were extruded from PLA, PETG, HDPE, and PA12 resins to achieve the maximum levels of coal filler content. PLA and PETG filaments were created with up to 40 wt % coal, and successful HDPE composite filaments were extruded containing up to 70 wt % coal. The PA12 composite filament was produced at 20 wt % coal for comparison to the processability of CPCs at commercial chopped carbon fiber loadings, and PA12 filaments were successfully produced with up to 30 wt % coal.

Figures S4−S7 show representative strands of the CPC filaments. The CPC filaments were extruded using the same extrusion parameters as those for the respective neat plastics. All CPC filaments exhibited smooth surface finishes comparable to those of the neat plastic filaments and were extruded within the acceptable tolerances for commercially available printers. HDPE-based filaments required the addition of a 1 wt % TPW-104 lubricant to achieve a smooth surface finish and consistent filament diameter.[46] Additionally, the composites did not show macroscale porosity or agglomeration throughout the microstructure (Section 3.1.2).

The CPC filaments were 3D printed into mechanical test samples. Examples of 3D printed CPC samples are provided in Figures S8−S11. The CPC filaments were processed using the same printing parameters as the respective unfilled plastics, demonstrating compatibility with existing AM techniques, which might lead to fast commercial adoption of the technology. In addition, CPC materials were processed using the same nozzle size and printing speeds utilized for common AM plastics, indicating similar manufacturing times for any given object and affinity with established AM processes.

The printability of the HDPE-based composites was impacted the most by the introduction of coal. Figure 1 shows images of additively manufactured virgin HDPE and
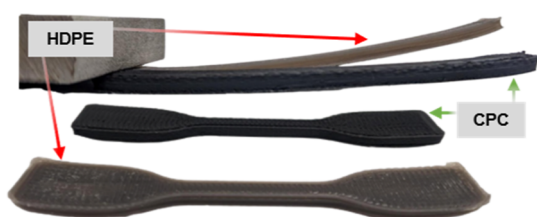
Figure 1. 3D printed HDPE-based CPC samples (shown with 50 wt % coal) exhibited reduced warping compared to unfilled HDPE prints.

HDPE-based composites with 50 wt % P8 coal. The neat HDPE flexural samples exhibited an average deflection from warping of 0.12 mm/mm along the axial length of the sample. When printed with 50 wt % coal, the average deflection of the HDPE composite reduced by 59.5% to 0.05 mm/mm along the axial length of the sample. The reduced deflection from warping resulted in greater dimensional accuracy of the printed parts. Increasing P8 content significantly reduced the warping of the HDPE prints and helped to overcome one of the key challenges limiting the utilization of HDPE in AM applications. Resolving the warping issues associated with the AM of HDPE allows for the utilization of more widely available and inexpensive plastics compared to the plastics readily used in current commercial technologies (i.e., PLA and PETG). In addition, reduced warping allowed for additive fabrication outside of a heated chamber, suggesting lower energy usage and higher dimensional stability of the HDPE-based composites in comparison to neat HDPE.

It was successfully demonstrated that CPC materials including formulations with a high filler content (up to 70 wt % P8 coal) could be integrated with several types of commercially available 3D printers without processing issues or the need for equipment modifications. The utilization of HDPE-based CPC materials in targeted applications such as additive housing construction and composite tooling is projected to substantially reduce manufacturing and material costs, reduce waste, minimize secondary operations during printing (curing and postcuring for thermoset-based AM and space heating for thermoplastic-based AM), increase dimensional stability, increase service life,[15] lower embodied energy and emissions,[13] and reduce manufacturing lead time.

3.1.2. Composite Microstructure. Optical microscopy was used to evaluate the microstructure of the CPC filaments. Figure 2 shows a representative example of CPC filament
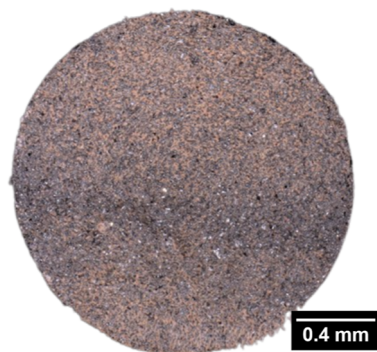

Figure 2. Representative microstructure of the HDPE-based composite filament with 60 wt % coal showing no porosity or agglomeration.

microstructures. The HDPE filament with 60 wt % P8 coal shows no porosity throughout the filament cross-section at ×150 magnification. Furthermore, the composite filaments exhibited even dispersion of the coal particles throughout the matrix with minimal regions of agglomeration. Images of all CPC filament microstructures are shown in Figures S12−S15.

Figure 3 shows representative tensile stress−strain curves of the four different CM polymer composites. As-fractured tensile
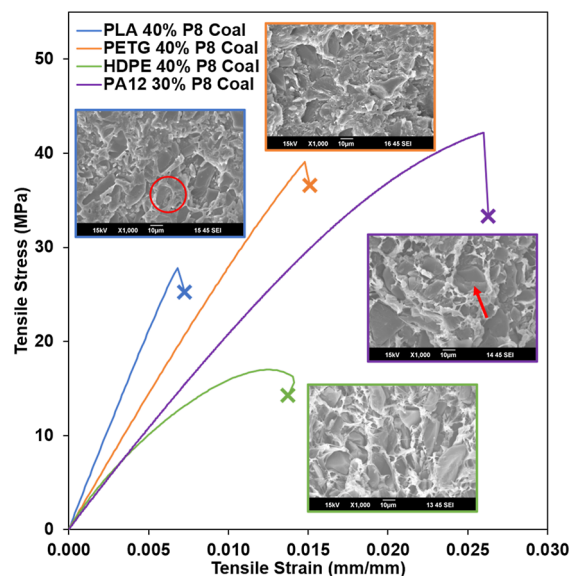

Figure 3. Representative composite tensile stress−strain curves with fractured surface SEM images showing particle pull-out (red circle) and coal particle fracture (red arrow) failure mechanisms.

and flexural samples were investigated by using SEM to evaluate particle−matrix interfaces and failure mechanisms in the composites. CPCs at different filler contents demonstrated comparable microstructures and failure mechanisms that were well represented by the SEM images shown in Figure 3. Figure 3 shows the SEM images for the PLA, PETG, and HDPE composites loaded at 40 wt % coal for direct comparison. The image and stress−strain curve for the PA12 composite is shown for the 30 wt % coal material because 30 wt % was the maximum coal loading achieved for the PA12 matrix which is most comparable to the other composites presented. While the matrix polymer had the greatest effect on the local microstructure, all four polymer materials showed minimal instances of porosity at the particle−matrix interface as the coal particles were well encased by the plastic. The fractured surfaces of these composites demonstrate two primary failure mechanisms.

CM samples showed instances of both particle pull-out (red circle) and particle fracture (red arrow), as shown in Figure 3. Particle pull-out was the primary failure mechanism in the PLA, PETG, and HDPE composites, and pull-out locations were readily visible throughout all four polymer composites. Additionally, instances of coal particle fracture indicated that the load was efficiently transferred from the matrix material to the particle filler. Alternatively, coal particle fractures could have been induced during material processing. While particle fractures were present in all four composites, the PA12 composites demonstrated a greater abundance of particle fracture locations. The particle fracture sites further indicate a

beneficial interaction between PA12 and the reinforcing coal particle (Section 3.2.3.).

The stress−strain curves of the PLA and PETG composites demonstrated a linear elastic response followed by a brittle fracture. The SEM images showed smooth, glossy fracture surfaces, confirming the brittle failure of the composites. Originally, the neat PLA and PETG materials exhibited ductile failures, with regions of plastic deformation after a yield point. The neat plastics possessed greater strain to failure than the respective CPCs. The HDPE and PA12 composites exhibited a yield point and possessed a small region of ductile plastic deformation prior to failure. In the SEM images (Figure 3), the polymer portions of the HDPE and PA12 composites show fibrillated strands of the polymer matrix which have undergone ductile deformation during testing. The yielding of the plastic around the coal particles results in a more ductile response seen in the stress−strain curves. In comparison, the neat HDPE material demonstrated a similar mechanical response but had a greater strain to failure and, thus, a larger region of plastic deformation than the composite. The neat PA12 and PA12 composites exhibited comparable stress−strain relations and strains to failure.

3.1.3. Tensile Properties. Tensile properties, shown in Figure 4, of the 3D printed (3DP) composite materials were determined and compared with those of the CM composites. Comparing the mechanical response of the 3DP composites to

the performance of the traditionally manufactured (i.e., CM) composites provides insights into the effects of the AM process. Furthermore, investigating CM CPCs establishes a benchmark of the isotropic performance of the intrinsic filament material prior to use in the 3D printing process which could introduce anisotropic responses due to layer orientations and print raster angles. The 3DP and CM samples exhibited analogous trends in tensile performance with respect to coal loading. As expected, the ultimate tensile strength (UTS) of the PLA, PETG, and HDPE composites decreased with an increase in coal content. The 3DP PLA composites exhibited a 38.6% decrease in UTS from 53.6 to 32.9 MPa at 40 wt % coal loading, and the 3DP PETG composites showed a 42.4% decrease in UTS from 52.9 to 30.5 MPa at 40 wt % coal loading. The UTS of the HDPE composites was impacted to a lesser extent by the introduction of coal. At 40 wt % coal, the UTS of the 3DP HDPE composite decreased 24.3% from 17.0 to 12.9 MPa. At 70 wt % coal, the UTS of the 3DP HDPE decreased to 9.5 MPa or 44.4% of the neat plastic strength. The reduction of UTS at high coal loadings could be attributed to particle agglomeration and weak coal-plastic interfacial bonding. Additionally, simulation results (Section 3.2.2.) showed little chemical interaction between the PLA, PETG, and HDPE and the P8 coal, making the composite analogous to a physical mixture. Weak interfacial bonding led to an increased number of stress concentration sites throughout the polymer matrix which provoked particle pull-out into being the most frequent failure mechanism in these composites (Section 3.1.2.). Akin to previous work, the strength of the composite exhibited a decreasing trend as more filler was introduced.[47−49]

The PA12 composites exhibit remarkably different behavior. The 3DP PA12 samples with 20 wt % coal loading demonstrated an increase in UTS from 28.9 to 30.4 MPa. The UTS of CM PA12 had the greatest response to coal introduction. The neat CM PA12 demonstrated an UTS of 32.1 MPa. However, when loaded with 20 wt % P8 coal, the CM PA12 composite exhibited a 45.2% increase in UTS, reaching a peak tensile strength of 46.6 MPa. These results are in agreement with previously published literature regarding the reinforcing effect of carbon and coal fillers in polyamide-based composite materials.[17,50] Enhanced UTS for the PA12-based composites could be attributed to improved interfacial bonding between coal and PA12, leading to an efficient load transfer from the polymer to the coal particle. Molecular simulations (Section 3.2.3.) and FTIR results (Section 3.2.3) further discuss the chemical bonding between the PA12 and the coal particles.

EM of all CPC materials showed increasing trends with increasing coal contents for both the 3DP and CM materials. Most notably, the 3DP HDPE composites exhibited a 340.6% increase in EM from 0.5 to 2.2 GPa from the neat plastic to 70 wt % coal. The stiffness of the PLA composites was the least impacted as the 3DP material only showed a 12.9% increase in the EM at 30 wt % coal. The 3DP PETG composites showed a 20.7% increase in EM at 40 wt % coal, and the 3DP PA12 composites showed a 42.5% increase in EM at 30 wt % coal. The increases in EM can be attributed to two primary factors: (1) the coal particles are stiffer than the matrix polymer, increasing the stiffness of the resulting composite, and (2) the increase in filler content reduced polymer chain mobility throughout the composite material. Similar trends have been reported for particulate-filled polymer composites.[12,47,49−51]
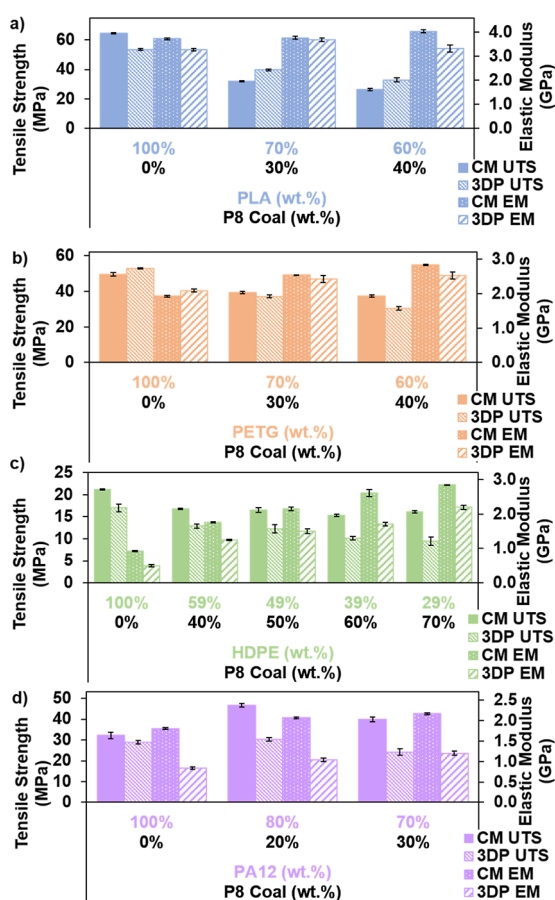

Figure 4. UTS and elastic modulus (EM) of 3DP and CM composites, including (a) PLA-based composites, (b) PETG-based composites, (c) HDPE-based composites, and (d) PA12-based composites. Error bars represent the standard error.

3.1.4. Flexural Properties. Flexural properties of the 3DP and CM CPCs are shown in Figure 5. The flexural properties
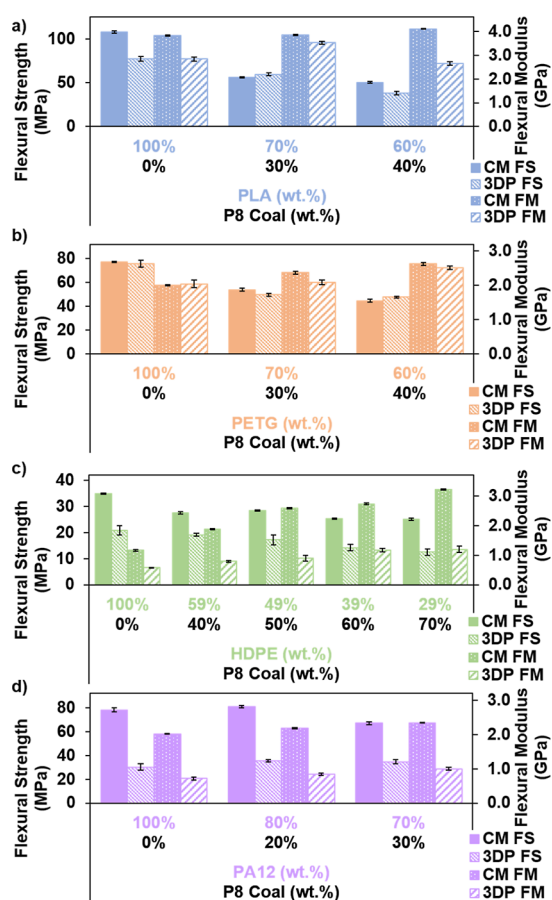

Figure 5. FS and FM of 3DP and CM composites, including (a) PLA-based composites, (b) PETG-based composites, (c) HDPE-based composites, and (d) PA12-based composites. Error bars represent the standard error.

of the composite materials reflect analogous trends to the tensile properties with respect to coal content. Flexural strength (FS) of both the CM and 3DP materials showed inverse proportionality with coal content for the PLA-, PETG-, and HDPE-based composites. The 3DP PLA composites demonstrated a 50.5% decrease in FS from 77.2 to 38.2 MPa at 40 wt % coal, and the 3DP PETG composites demonstrated a 36.9% decrease in FS from 75.5 to 47.7 MPa at 40 wt % coal. As observed with the UTS, the 3DP HDPE composite strengths were less sensitive to the introduction of coal, and at 40 wt % coal, the 3DP HDPE composite showed only an 8.3% decrease in FS from 20.9 to 19.1 MPa. At 70 wt % coal loading, the CM HDPE composite displayed a 28.1% decrease in FS. Previous research showed similar FS trends with the introduction of particulate fillers in polymer matrices.[49] The reduction of the FS values was primarily due to agglomeration and weak interfacial bonding.

Similar to the tensile properties, the PA12 composites demonstrated a FS increase with the introduction of coal. 3DP PA12 composites exhibited a 16.9% increase in FS from 30.2 MPa to a peak FS of 35.3 MPa at 20 wt % coal loading. This increase was attributed to improved interfacial bonding between the coal and PA12 (Section 3.2.3.).

The flexural modulus (FM) of all CPC materials increased with the increase in coal content. At 40 wt % coal, the CM PLA composites showed a slight 7.3% increase in FM from 3.8 to 4.1 GPa analogous to the PLA EM behavior. The 3DP PETG composites exhibited a 23.0% increase in FM from 2.0 to 2.5 GPa at 40 wt % coal, and the 3DP PA12 composites demonstrated a 39.3% increase in FM from 0.7 to 1.0 GPa at 30 wt % coal. HDPE composite stiffness had the most significant response to coal introduction. The 3DP HDPE composites at 70 wt % coal showed a 105.6% increase in FM to 1.2 GPa, and the CM HDPE composites at 70 wt % showed a 176.6% increase in FM to 3.2 GPa. Similar trends have been reported in the literature where the higher stiffness values were attributed to stiffer particles and limited polymer chain mobility.[12,13]

3.1.5. Impact Resistance. Notched Izod impact resistance was determined for the 3DP and CM CPC materials. Figure 6
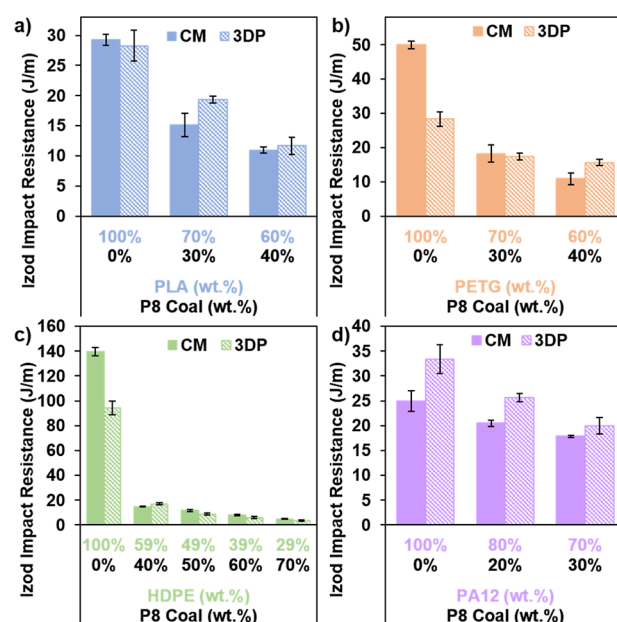

Figure 6. Izod impact resistance of 3DP and CM composites, including (a) PLA-based composites, (b) PETG-based composites, (c) HDPE-based composites, and (d) PA12-based composites. Error bars represent the standard error.

shows the impact resistances of the composite materials at different coal contents. For all matrix polymers, the impact resistance of the composite decreased with filler content for the 3DP and CM materials. The 3DP PA12 composites exhibited a 40.1% decrease in impact resistance from 33.4 to 20.0 J m^{-1} at 30 wt % coal. Similarly, the 3DP PLA and PETG composites exhibited a 58.7 and 44.6% decrease, respectively, in impact resistance at 40 wt % coal. The HDPE composites exhibited the greatest decrease in impact resistance with the introduction of coal. The 3DP HDPE composites exhibited an 82.0% decrease in impact resistance from 94.2 to 16.9 J m^{-1} at 40 wt % coal, and the 3DP impact resistance continued to decrease to 3.4 J m^{-1} at 70 wt % coal. Previous work with particulate-filled polymer composites showed similar impact resistance trends.[49] Increased particle loading resulted in a greater coal−polymer interface surface area, therefore enhancing crack initiation and propagation.

3.1.6. Hardness. Figure 7 shows that the CPC materials demonstrated increasing Shore D hardness with coal content
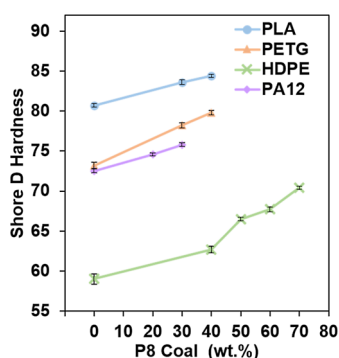

Figure 7. Shore D hardness of CM composites, including PLA-based, PETG-based, HDPE-based, and PA12-based composites. Error bars represent the standard error.

due to the introduction of a filler material harder than the matrix. Previous studies have shown that polymer composites with harder particulate filler materials exhibited comparable tendencies.[52] Most notably, the HDPE composites demonstrated a 19.3% increase from a neat plastic hardness of 59.0 to a hardness of 70.4 at 70 wt % coal loading. The increased hardness of the composites improved the FDM of the HDPE filaments. Due to the neat HDPE's low hardness, the FDM printer's extruder wheel caused significant filament abrasion, resulting in underextruded material and failed prints. Conversely, the harder composite filament resisted abrasion and improved the printing reliability. The PLA and PETG composites showed a respective increase in hardness of 4.6 to 84.4% and 9.0 to 79.8% at 40 wt % coal. Similarly, the PA12 composites exhibited a 4.6% increase in hardness from 72.5 to 75.8 at 30 wt % coal.

3.2. Simulation Results. *3.2.1. P8 Coal Chemical Structure Validation.* To analyze the local conformation of the coal model, an ab initio multiple-scattering calculation of the extended X-ray absorption fine structure (EXAFS) was performed using the real-space Green's function code FEFF10.[53] The K-edge of sulfur was studied, and the extracted postedge oscillations $[\chi(E)]$ were Fourier transformed (FT)

into real space using the Kaiser windowing function with $\beta = 2$.[54] The resulting spectrum provides the radial distribution function (RDF). The peaks of the normalized Fourier amplitude obtained for the coal model were compared with experimental data from Huffman and co-workers.[55] The peak positions from this study were found to be in close agreement with the FTIR experimental values. The positions of the first, second, and third peaks from this work (ref. 55) were 1.74 Å (1.75 Å), 3.04 Å (2.84 Å), and 3.99 Å (4.02 Å), respectively. This confirms that the coal models used in this study reasonably predict the structure of the bituminous coal. The EXAFS spectra for the P8 coal model are provided in Figure S16 of the Supporting Information.

3.2.2. Coal-Plastic Interfacial Phenomena. Molecular simulations of the coal models at the experimental processing temperature were performed to gain insights into possible bond-breaking and bond-forming sites in the coal. The interactions in the models were investigated by calculating the bond order per atom and chemical species at specific intervals during the simulation. At the beginning of each simulation, the number of coal and plastic molecules was known, and the bond order and available chemical species provided information on intra- and intermolecular interactions.

Figure 8 provides an illustration of the bond-breaking sites in the P8 coal model. The coal macromolecules are generally seen to break down into three subunits, represented by green, teal, and magenta clusters. The bond-breaking sites, highlighted in black circles in Figure 8, were identified as the self-associated OH hydrogen bonds between two phenol-hydroxides (ph-OH) in the P8 coal. The chemical formulas of the coal subunits, along with their associated colors in Figure 8, are $C_{105}H_{88}O_{10}N_2S_2$ (green), $C_{42}H_{34}O_4$ (teal), and $C_{19}H_{16}O$ (magenta). Interestingly, CH_3 and H_2 were released in about 14% of the simulation realizations at an early stage of heating. The CH_3 fragments result from the breaking of the ethylene bridges during the thermal process, which is also observed experimentally during P8 coal pyrolysis.[31,56,57]

The interfacial phenomena between coal and PLA, PETG, and HDPE in the composites were investigated, and the results are illustrated in Figures S18−S20. After 5 ns of heating, the configuration of the system revealed that the molecules tend to aggregate and form clusters without observable evidence of
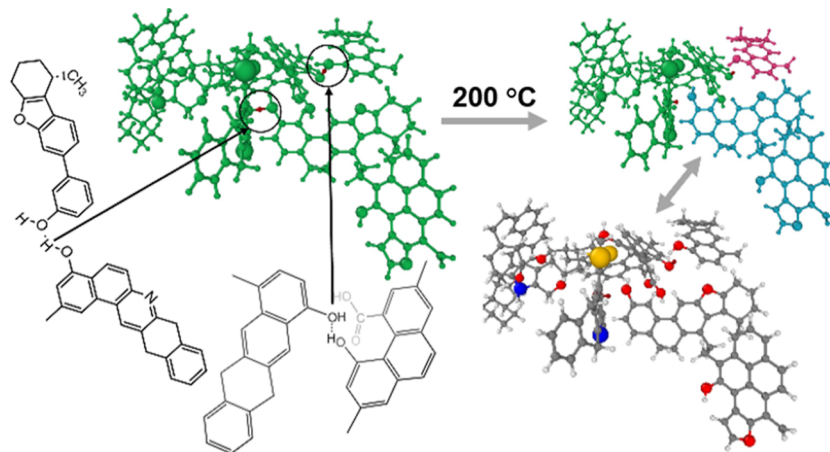

Figure 8. Bond-breaking sites found in the coal model at 200 °C. The bonds break at the region with weaker noncovalent bonds (hydrogen bonding). The hydrogen bonds hold the different subunits of the different coal macromolecules together. The chemical structures of the cleaved subunits are indicated in different colors: $C_{105}H_{88}O_{10}N_2S_2$ (green), $C_{42}H_{34}O_4$ (teal), and $C_{19}H_{16}O$ (magenta).

chemical bonding. This suggests that the equilibrium state of the heterogeneous matrix involves purely physical mixing without intermolecular bonding. This simulation data supports the experimental observation of the negative impact of coal on the UTS and FS for the composites made using PLA, PETG, and HDPE polymers. However, it is worth noting that PA12 showed different behavior in the simulation, indicating that it may have beneficial interfacial phenomena (i.e., chemical bonding) with coal, leading to improved mechanical properties.

3.2.3. Hydrogen Bonding in PA12-Based Composites.

Both the widely accepted structural models of coal, namely, the host−guest model[58,59] and the associated model,[60] have extensively investigated the impact of noncovalent bonds, such as van der Waals forces, hydrogen bonding, ionic linkages, and π−π interactions, on the chemical structure of coal.[61−65] Studies by Larsen and co-workers estimated that noncovalent bonds surpass the number of covalent cross-links by a factor of 4 in coal,[66] and specifically for P8 coal, it was suggested that approximately 0.3 cross-linking hydrogen bonds are present per 100 carbon atoms.[67] Additionally, Brenner demonstrated that hydrogen bonding likely contributes to the high glass transition temperature and glassy properties observed in bituminous coal.[68] Molecular simulations of the interaction between PA12 and P8 coal revealed prevalent forms of hydrogen bonding between the hydroxide (OH) in the phenolic group of coal (ph-OH) and the amide group (−NH−C=O$^-$) in PA12.

Figure 9 provides visual representations of hydrogen bond formation in the PA12 composite material. Figure 9a displays snapshots of the local environment before and after the formation of hydrogen bonding between the strong proton donor ph-OH in coal and the strong proton acceptor oxygen in the amide group. In some instances, double hydrogen bonds

were observed,[69] as shown in Figure 9b. The hydrogen bond lengths ranged from 1.61 to 1.86 Å. A proposed mechanism for the hydrogen bonding observed in the PA12-coal composite is that it results from the high polarity of the amide linkages along the polyamide chain, as depicted in eq 1

$$\text{(1)}$$

The rigidity and planarity of the amide linkage induce a positive and negative charge on the nitrogen and oxygen atoms, respectively, facilitating π-bond cooperativity, also known as resonance-assisted hydrogen bonding (RAHB).[69] In RAHB, the polarization occurs by charge flow through the π bonds. The N−H in the amide group becomes a stronger donor if the amide O atom accepts a hydrogen bond (i.e., Ph-OH⋯O=C−N−H), as portrayed in Figure 9b, resulting in a stabilized zwitterionic resonance.[69] Except for HDPE, which is nonpolar, both PLA and PETG, like PA12, possess polar functional groups (COOH in PLA and OH in PETG) capable of forming H-bonds. However, the closely packed nonpolar carbon backbone in these polymers (i.e., the methyl group in the PLA monomers and the cyclohexanes and benzene aromatic structures in PETG monomers) induces steric congestion, which can significantly reduce the reactivity (H-bonding) of the polar functional groups in these materials. In contrast, PA12 features a longer linear backbone with 12 carbon atoms, leading to less steric hindrance. Consequently, PA12 exhibits higher conformational flexibility, enabling its molecules to adopt desired spatial rearrangements.

The presence of hydrogen bonding between PA12 and P8 coal in the composite was validated experimentally through FTIR analysis. The FTIR spectra obtained for the PA12 composites (Figure 9c) were normalized to the C−H peak, assuming that the C−H bonds along the PA12 molecule remained constant during the composite compounding process. The spectra for the composite materials with 0, 20, and 30% coal are shown in black, green, and orange, respectively. No new peak formations or disappearances were observed with the introduction of coal, suggesting that no covalent bonds exist between PA12 and coal.

However, a notable decrease in the N−H in-plane bending peak at ≈1557 cm^{-1} was observed with the addition of coal, as shown in the inset in Figure 9c, yet the N−H stretching peak at ≈3284 cm^{-1} remained unchanged. The absence of a new peak for covalent bonding, combined with the results obtained from the simulations, suggests that the reduction in the N−H in-plane bending peak could be attributed to the formation of hydrogen bonding, which constrains the mobility of the initially free N−H bond. The presence of hydrogen bonding throughout the composite allows the coal particles to act as reinforcing fillers, as demonstrated by the experimental tensile and flexural results. The formation of hydrogen bonds between PA12 and coal particles enhances the interfacial adhesion and overall mechanical performance of the composite.

Figure 9. Hydrogen bonding in the simulation models and FTIR spectra of PA12 composites. A snapshot before and after bonding is shown in (a) and (b) representative double hydrogen bonding between the (1) oxygen and (2) nitrogen in the amide group in PA12 (−NH−C=O$^-$) and (3) oxygen in the phenolic group (ph-OH) of the coal. The FTIR spectra of PA12 composites are shown in (c). In (b), all hydrogen atoms except the polar hydrogens have been deleted for clarity.

4. CONCLUSIONS

In this work, bituminous P8 coal was incorporated as a particulate filler in thermoplastic-based composites to develop 1.75 mm diameter filaments for utilization in FDM printing.
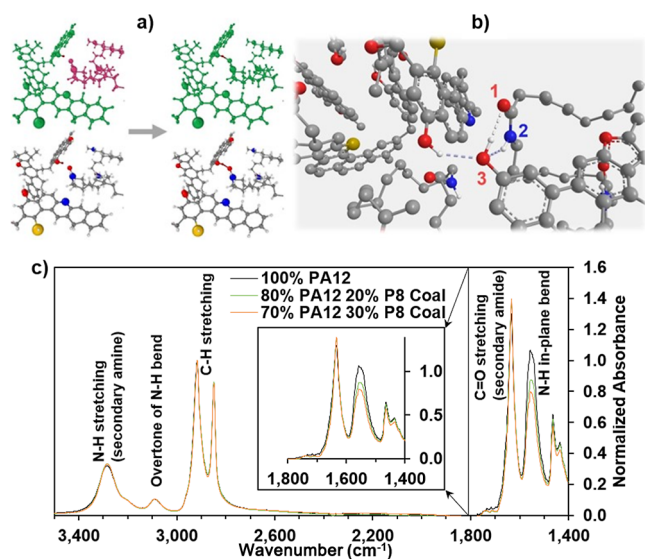
The composites, composed of PLA, PETG, HDPE, and PA12 resins with coal loadings of 20 to 70 wt %, were evaluated for their tensile properties, flexural properties, and Izod impact resistance in both 3DP and CM states. CPC filaments were extruded and 3D printed by using the same processing parameters as the respective neat plastics. The introduction of coal significantly reduced warping in HDPE-based prints, thus addressing a serious problem and providing a viable avenue to additively manufacture HDPE parts. The resulting CPCs exhibited increased moduli and improved tensile and flexural strength in the PA12 composite, but all materials demonstrated a decreasing impact resistance with a coal content. Analysis of failure mechanisms revealed particle pull-out and particle fracture as the dominant failure modes, and the composite hardness increased with coal content. Atomistic models of the polymers and P8 coal were created to simulate their interactions. PA12 CPC simulations revealed hydrogen bonding between the polymer and the coal molecules. The hydrogen bonding between PA12 and P8 coal formed between the hydroxide (OH) in the phenolic group of P8 coal (ph-OH) and the amide group ($-NH-C=O^-$) in PA12. The formation of hydrogen bonds in PA12 CPC materials was supported by FTIR spectra and provided a possible basis for the enhanced mechanical performance of the composite. These findings, along with the development of CPC filaments and supporting molecular simulations, demonstrate a viable avenue for FDM printing of CPC components and structures.

■ ASSOCIATED CONTENT

ⓢ Supporting Information

The Supporting Information is available free of charge at https://pubs.acs.org/doi/10.1021/acsapm.3c01784.

> CPC printing parameters; representative simulation models; composite filaments; 3D printed composite samples; composite filament microstructure; and some simulation results for the PLA, PETG, and HDPE composite models (PDF)

■ AUTHOR INFORMATION

Corresponding Authors

Logan E. Veley − *Institute for Sustainable Energy and the Environment (ISEE), Department of Chemical and Biomolecular Engineering, Ohio University, Athens, Ohio 45701, United States; Department of Mechanical Engineering, Ohio University, Athens, Ohio 45701, United States;* ⓞ orcid.org/0000-0002-4555-1637; Email: lv199716@ohio.edu

Yahya Al-Majali − *Institute for Sustainable Energy and the Environment (ISEE), Department of Chemical and Biomolecular Engineering, Ohio University, Athens, Ohio 45701, United States; Department of Mechanical Engineering, Ohio University, Athens, Ohio 45701, United States;* Email: almajali@ohio.edu

Authors

Chinonso Ugwumadu − *Department of Physics and Astronomy, Nanoscale and Quantum Phenomena Institute (NQPI), Ohio University, Athens, Ohio 45701, United States;* ⓞ orcid.org/0000-0001-9920-7594

Jason P. Trembly − *Institute for Sustainable Energy and the Environment (ISEE), Department of Chemical and Biomolecular Engineering, Ohio University, Athens, Ohio*

45701, United States; Department of Mechanical Engineering, Ohio University, Athens, Ohio 45701, United States; ⓞ orcid.org/0000-0002-9851-2914

David A. Drabold − *Department of Physics and Astronomy, Nanoscale and Quantum Phenomena Institute (NQPI), Ohio University, Athens, Ohio 45701, United States*

Complete contact information is available at: https://pubs.acs.org/10.1021/acsapm.3c01784

Author Contributions

The manuscript was written through the contributions of all authors. All authors have given their approval to the final version of the manuscript.

Notes

The authors declare no competing financial interest.

■ ACKNOWLEDGMENTS

■ REFERENCES

(1) Ligon, S.; Liska, R.; Stampfl, J.; Gurr, M.; Mulhaupt, R. Polymers for 3D Printing and Customized Additive Manufacturing. *Chem. Rev.* **2017**, *117* (15), 10212−10290.

(2) Post, B.; Richardson, B.; Lind, R.; Love, L.; Lloyd, P.; Kune, V.; Rhyne, B.; Roschli, A.; Hannan, J.; Nolet, S.; Veloso, K.; Parthiv, K.; Remo, T.; Jenne, D. BIG AREA ADDITIVE MANUFACTURING APPLICATION IN WIND TURBINE MOLDS. In *Solid Freeform Fabrication Symposium*, 2017.

(3) Global Industry Analysts, Inc. *Composite Tooling - Global Strategic Business Report*, 2023; p 243. https://www.researchandmarkets.com/reports/4804211/composite-tooling-global-strategic-business.

(4) Wampol, C. *Additive Manufacturing with High Density Poly-ethylene: Mechanical Properties Evaluation*; South Dakota State University, 2018.

(5) Schirmeister, C. G.; Hees, T.; Licht, E. H.; Mülhaupt, R. 3D Printing of High Density Polyethylene by Fused Filament Fabrication. *Addit. Manuf.* 2019, 28, 152−159.

(6) Angelopoulos, P.; Samouhos, M.; Taxiarchou, M. Functional Fillers in Composite Filaments for Fused Filament Fabrication; a Review. *Mater. Proc.* 2021, 37 (4), 4031−4043.

(7) Wang, X.; Jiang, M.; Zhou, Z.; Gou, J.; Hui, D. 3D Printing of Polymer Matrix Composites: A Review and Prospective. *Composites, Part B* 2017, 110, 442−458.

(8) Aida, H.; Nadlene, R.; Mastura, M.; Yusriah, L.; Sivakumar, D.; Ilyas, R. Natural Fibre Filament for Fused Deposition Modelling (FDM): A Review. *Int. J. Sustain. Eng.* 2021, 14 (6), 1988−2008.

(9) Gardner, D.; Wang, L.; Wang, J. ADDITIVE MANUFACTUR-ING OF WOOD-BASED MATERIALS FOR COMPOSITE APPLICATIONS. *Proceedings of the SPE Automotive Composites Conference \& Exhibition, Novi, MI, USA*, 2019.

(10) Tao, Y.; Wang, H.; Li, Z.; Li, P.; Shi, S. Development and Application of Wood Flour-Filled Polylactic Acid Composite Filament for 3D Printing. *Materials* 2017, 10 (4), 339.

(11) Pervaiz, S.; Qureshi, T.; Kashwani, G.; Kannan, S. 3D Printing of Fiber-Reinforced Plastic Composites Using Fused Deposition Modeling: A Status Review. *Materials* 2021, 14 (16), 4520.

(12) Phillips, L.; Kappagantula, K.; Trembly, J. Mechanical Performance of Thermoplastic Composites Using Bituminous Coal as Filler: Study of a Potentially Sustainable End-Use Application for Appalachian Coal. *Polym. Compos.* 2019, 40 (2), 591−599.

(13) Al-Majali, Y.; Chirume, C.; Marcum, E.; Daramola, D.; Kappagantula, K.; Trembly, J. Coal-Filler-Based Thermoplastic Composites as Construction Materials: A New Sustainable End-Use Application. *ACS Sustain. Chem. Eng.* 2019, 7 (19), 16870−16878.

(14) Al-Majali, Y. T.; Trembly, J. P. Flammability and Thermal Stability of Thermoplastic-Based Composites Filled with Natural Carbon. *J. Fire Sci.* 2022, 40 (3), 175−193.

(15) Al-Majali, Y.; Forshey, S.; Trembly, J. Effect of Natural Carbon Filler on Thermo-Oxidative Degradation of Thermoplastic-Based Composites. *Thermochim. Acta* 2022, 713, 179226.

(16) Veley, L.; Trembly, J.; Al-Majali, Y. 3D Printing of Sustainable Coal Polymer Composites: Thermophysical Characteristics. *Mater. Today Commun.* 2023, 37, 106989.

(17) Zhang, S.; Rehman, M. Z. ur; Bhagia, S.; Meng, X.; Meyer, H. M.; Wang, H.; Koehler, M. R.; Akhtar, K.; Harper, D. P.; Ragauskas, A. J. Coal Polymer Composites Prepared by Fused Deposition Modeling (FDM) 3D Printing. *J. Mater. Sci.* 2022, 57 (22), 10141−10152.

(18) Thapa, R.; Drabold, D. Ab Initio Simulation of Amorphous Materials. *At. Simul. Glas. Fundam. Appl.* 2022, 2, 30−59.

(19) Daubeny, R. D. P.; Bunn, C. W.; Brown, C. J. The Crystal Structure of Polyethylene Terephthalate. *Proc. R. Soc. A* 1954, 226 (1167), 531−542.

(20) Inoue, K.; Hoshino, S. Crystal Structure of Nylon 12. *J. Polym. Sci., Polym. Phys. Ed.* 1973, 11 (6), 1077−1089.

(21) Thapa, R.; Ugwumadu, C.; Nepal, K.; Trembly, J.; Drabold, D. Ab Initio Simulation of Amorphous Graphite. *Phys. Rev. Lett.* 2022, 128 (23), 236402.

(22) Ugwumadu, C.; Nepal, K.; Thapa, R.; Drabold, D. Atomistic Nature of Amorphous Graphite. *Phys. Chem. Glasses: Eur. J. Glass Sci. Technol., Part B* 2023, 64 (1), 16−22.

(23) Ugwumadu, C.; Nepal, K.; Thapa, R.; Lee, Y.; Al-Majali, Y.; Trembly, J.; Drabold, D. Simulation of Multi-Shell Fullerenes Using Machine-Learning Gaussian Approximation Potential. *Carbon Trends* 2023, 10, 100239.

(24) Ugwumadu, C.; Thapa, R.; Al-Majali, Y.; Trembly, J.; Drabold, D. Formation of Amorphous Carbon Multi-Walled Nanotubes from Random Initial Configurations. *Phys. Status Solidi B* 2023, 260 (3), 2200527.

(25) Davidson, R. Molecular Structure of Coal. *Coal Sci.* 1982, 1, 83−160.

(26) Mathews, J.; Chaffee, A. The Molecular Representations of Coal - A Review. *Fuel* 2012, 96, 1−14.

(27) Wiser, W.; Conversion of Bituminous Coal to Liquids and Gases: Chemistry and Representative Processes*Magn. Reson.*; , 1984; Vol. 124.

(28) Wender, I. Catalytic Synthesis of Chemicals from Coal. *Catal. Rev.: Sci. Eng.* 1976, 14 (1), 97−129.

(29) Given, P. Structure of Bituminous Coals: Evidence from Distribution of Hydrogen. *Nature* 1959, 184, 980−981.

(30) Shinn, J. From Coal to Single-Stage and Two-Stage Products: A Reactive Model of Coal Structure. *Fuel* 1984, 63 (9), 1187−1196.

(31) Solomon, P. Relation Between Coal Structure and Thermal Decomposition Products. *Coal Struct.* 1981, 192, 95−112.

(32) Hanwell, M.; Curtis, D.; Lonie, D.; Vandermeersch, T.; Zurek, E.; Hutchison, G. Avogadro: An Advanced Semantic Chemical Editor, Visualization, and Analysis Platform. *J. Cheminf.* 2012, 4 (1), 17.

(33) Kresse, G.; Furthmuller, J. Efficient Iterative Schemes for Ab Initio Total-Energy Calculations Using a Plane-Wave Basis Set. *Phys. Rev. B: Condens. Matter Mater. Phys.* 1996, 54 (16), 11169−11186.

(34) van Duin, A.; Dasgupta, S.; Lorant, F.; Goddard, W. ReaxFF: A Reactive Force Field for Hydrocarbons. *J. Phys. Chem. A* 2001, 105 (41), 9396−9409.

(35) Allinger, N. L.; Yuh, Y. H.; Lii, J. H. Molecular Mechanics. The MM3 Force Field for Hydrocarbons. 1. *J. Am. Chem. Soc.* 1989, 111 (23), 8551−8566.

(36) ASTM International. *ASTM D638 Standard Test Method for Tensile Properties of Plastics*, 2014.

(37) ASTM International. *ASTM D790 Standard Test Methods for Flexural Properties of Unreinforced and Reinforced Plastics and Electrical Insulating Materials*, 2010.

(38) ASTM International. *ASTM D256 Standard Test Methods for Determining the Izod Pendulum Impact Resistance of Plastics*, 2018.

(39) Seery, D. *Investigation of the Devolatilization of Coal under Combustion Conditions*, Technical Report DOE/ET/10744-T1; United Technologies Research Center, 1980.

(40) Martinez, J.; Martinez, L. Packing Optimization for Automated Generation of Complex System's Initial Configurations for Molecular Dynamics and Docking. *J. Comput. Chem.* 2003, 24 (7), 819−825.

(41) Blochl, P. Projector Augmented-Wave Method. *Phys. Rev. B: Condens. Matter Mater. Phys.* 1994, 50 (24), 17953−17979.

(42) Perdew, J.; Burke, K.; Ernzerhof, M. Generalized Gradient Approximation Made Simple. *Phys. Rev. Lett.* 1996, 77 (18), 3865−3868.

(43) Thompson, A.; Aktulga, H.; Berger, R.; Bolintineanu, D.; Brown, W.; Crozier, P.; in 't Veld, P. J.; Kohlmeyer, A.; Moore, S.; Nguyen, T.; Shan, R.; Stevens, M.; Tranchida, J.; Trott, C.; Plimpton, S. LAMMPS - a Flexible Simulation Tool for Particle-Based Materials Modeling at the Atomic, Meso, and Continuum Scales. *Comput. Phys. Commun.* 2022, 271, 108171.

(44) Nose, S. A Molecular Dynamics Method for Simulations in the Canonical Ensemble. *Mol. Phys.* 1984, 52 (2), 255−268.

(45) Hoover, W. Canonical Dynamics: Equilibrium Phase-Space Distributions. *Phys. Rev. A* 1985, 31 (3), 1695−1697.

(46) Struktol Company of America, LLC. *STRUKTOL TPW 104*, 2016; https://struktol.com/fileadmin/user_upload/Products/PDF/TD_TPW104.pdf.

(47) Atikler, U.; Basalp, D.; Tihminlioglu, F. Mechanical and Morphological Properties of Recycled High-Density Polyethylene,

Filled with Calcium Carbonate and Fly Ash. *J. Appl. Polym. Sci.* **2006**, *102* (5), 4460−4467.

(48) Battegazzore, D.; Noori, A.; Frache, A. Natural Wastes as Particle Filler for Poly(Lactic Acid)-Based Composites. *J. Compos. Mater.* **2018**, *53* (6), 783−797.

(49) Dobrosielska, M.; Dobrucka, R.; Brzakalski, D.; Frydrych, M.; Kozera, P.; Wieczorek, M.; Jalbrzykowski, M.; Kurzydlowski, K.; Przekop, R. E. Influence of Diatomaceous Earth Particle Size on Mechanical Properties of PLA/Diatomaceous Earth Composites. *Materials* **2022**, *15* (10), 3607.

(50) Athreya, S.; Kalaitzidou, K.; Das, S. Mechanical and Microstructural Properties of Nylon-12/Carbon Black Composites: Selective Laser Sintering versus Melt Compounding and Injection Molding. *Compos. Sci. Technol.* **2011**, *71* (4), 506−510.

(51) Fu, S.-Y.; Feng, X.-Q.; Lauke, B.; Mai, Y.-W. Effects of Particle Size, Particle/Matrix Interface Adhesion and Particle Loading on Mechanical Properties of Particulate-Polymer Composites. *Composites, Part B* **2008**, *39* (6), 933−961.

(52) Georgopoulos, S.; Tarantili, P.; Avgerinos, E.; Andreopoulos, A.; Koukios, E. Thermoplastic Polymers Reinforced with Fibrous Agricultural Residues. *Polym. Degrad. Stab.* **2005**, *90* (2), 303−312.

(53) Kas, J.; Vila, F.; Pemmaraju, C. D.; Tan, T. S.; Rehr, J. J. Advanced Calculations of X-Ray Spectroscopies with FEFF10 and Corvus. *J. Synchrotron Radiat.* **2021**, *28*, 1801−1810.

(54) Kaiser, J.; Kuo, F. Digital Filters. *System Analysis by Digital Computer*; Wiley, 1966.

(55) Huffman, G. P.; Huggins, F. E.; Mitra, S.; Shah, N.; Pugmire, R. J.; Davis, B.; Lytle, F. W.; Greegor, R. B. Investigation of the Molecular Structure of Organic Sulfur in Coal by XAFS Spectroscopy. *Energy Fuels* **1989**, *3* (2), 200−205.

(56) Bent, R.; Ladner, W.; Joy, W. ESTIMATE OF METHYL GROUPS IN COALS+ COAL DERIVATIVES. *Fuel* **1964**, *43* (1), 5.

(57) Mazumdar, B. Hydrogen in Coal: Part 1. Genetic and Structural Development. *Fuel* **1972**, *51* (4), 284−289.

(58) Solomon, P.; Fletcher, T.; Pugmire, R. Progress in Coal Pyrolysis. *Fuel* **1993**, *72* (5), 587−597.

(59) Lynch, L.; Sakurovs, R.; Webster, D.; Redlich, P. 1H n.m.r. Evidence to Support the Host/Guest Model of Brown Coals. *Fuel* **1988**, *67* (8), 1036−1041.

(60) Nishioka, M. The Associated Molecular Nature of Bituminous Coal. *Fuel* **1992**, *71* (8), 941−948.

(61) Marzec, A. Macromolecular and Molecular Model of Coal Structure. *Fuel Process. Technol.* **1986**, *14*, 39−46.

(62) Larsen, J. W.; Green, T. K.; Kovac, J. The Nature of the Macromolecular Network Structure of Bituminous Coals. *J. Org. Chem.* **1985**, *50* (24), 4729−4735.

(63) Painter, P.; Sobkowiak, M.; Youtcheff, J. FT-i.r. Study of Hydrogen Bonding in Coal. *Fuel* **1987**, *66* (7), 973−978.

(64) Chen, C.; Gao, J.; Yan, Y. Observation of the Type of Hydrogen Bonds in Coal by FTIR. *Energy Fuels* **1998**, *12* (3), 446−449.

(65) Li, D.; Li, W.; Li, B. A New Hydrogen Bond in Coal. *Energy Fuels* **2003**, *17* (3), 791−793.

(66) Larsen, J.; Lee, D.; Shawver, S. Coal Macromolecular Structure and Reactivity. *Fuel Process. Technol.* **1986**, *12*, 51−62.

(67) Larsen, J. W.; Gurevich, I.; Glass, A. S.; Stevenson, D. S. A Method for Counting the Hydrogen-Bond Cross-Links in Coal. *Energy Fuels* **1996**, *10* (6), 1269−1272.

(68) Brenner, D. The Macromolecular Nature of Bituminous Coal. *Fuel* **1985**, *64* (2), 167−173.

(69) Steiner, T. The Hydrogen Bond in the Solid State. *Angew. Chem., Int. Ed.* **2002**, *41* (1), 48−76.